Renewable Energy 277 (2026) 126549

Contents lists available at ScienceDirect

Renewable Energy

journal homepage: www.elsevier.com/locate/renene

Numerical investigation of heat extraction performance of a multi-casing coaxial well with multilateral branches for enhanced geothermal systems

Guoying Wang [a,b], Xingyu Liu [a], Guofeng Song [c,*], Wenyuan Jiang [d], Housheng Jia [a,b], Songlin Guo [a], Norbert Klitzsch [e], Chuanliang Yan [f], Shaowei Liu [a,b]

[a] School of Energy Science and Engineering, Henan Polytechnic University, Jiaozuo, 454002, China
[b] State Collaborative Innovation Center of Coal Work Safety and Clean-efficiency Utilization, Henan Polytechnic University, Jiaozuo, 454002, China
[c] Department of Geoscience and Engineering, Delft University of Technology, Delft, 2628CN, the Netherlands
[d] School of Mechanical Engineering, Shandong University, Jinan, 250100, China
[e] Institute for Applied Geophysics and Geothermal Energy, RWTH Aachen University, Aachen, 52074, Germany
[f] Key Laboratory of Unconventional Oil & Gas Development (China University of Petroleum (East China)), Ministry of Education, 266580, China

ARTICLE INFO

Keywords:
Enhanced geothermal system
Multi-casing coaxial well
Multilateral branches
Heat extraction
Fracture
Thermo-hydro-mechanical coupling

ABSTRACT

A novel enhanced geothermal system is proposed using a multi-casing coaxial well with multilateral branches, where a single main wellbore with three concentric pipes separates the injection zone from two production zones. This configuration creates two independent production zones, significantly expanding the heat exchange volume and improving overall heat extraction efficiency. A three-dimensional fully coupled thermo-hydro-mechanical numerical model was established to systematically simulate the heat extraction performance of the newly proposed system and compare it with a conventional Enhanced Geothermal System using a single-casing coaxial well with multilateral branches. The results show that the cumulative power of the newly proposed system increases by approximately 14%-52% compared to the conventional one under different fracture densities over a 60-year operation period. The pressure difference between the injection well and production well decreases by 81%-94%. Parametric analysis reveals that heat extraction efficiency is further improved by controlling the fracture dimensions, selecting an appropriate number of branches, maximizing the length of the branches, and adjusting the injection rate. Furthermore, economic analysis shows that the newly proposed system can significantly reduce the levelized cost of energy compared with conventional systems. This research proposes an alternative enhanced geothermal design that significantly improves heat extraction performance.

1. Introduction

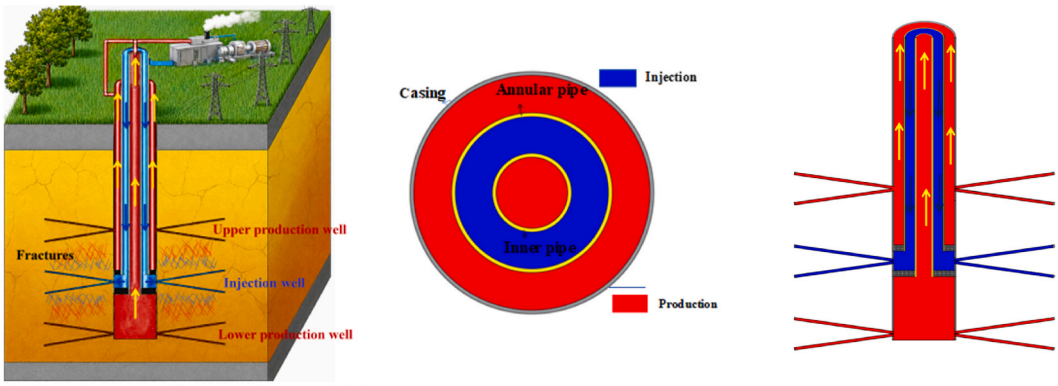
Geothermal energy is regarded as a viable alternative to fossil energy during energy transition as it is clean, stable, environmentally friendly, and widely distributed. Hot dry rock, as one of the major forms of geothermal resources, shows significant potential for heating and power generation. It refers to rock masses buried 3-10 km below the surface, containing little or no fluid, and with temperatures above 180 °C [1]. Because of its enormous thermal potential, wide geographical distribution, and environmentally sustainable characteristics, hot dry rock has attracted increasing attention from both governments and academia worldwide [2].

Due to the low porosity and low permeability of hot dry rock, it is difficult to form effective fluid circulation channels under natural conditions. The development of hot dry rock resources mainly relies on enhanced geothermal system (EGS) technology [4]. Conventional EGSs generally use doublet or multi-well configurations and create an artificial fracture network between wells through hydraulic fracturing [5]. The working fluid circulates through the fractures and extracts heat, thereby realizing geothermal energy extraction [6]. For example, demonstration projects such as FORGE in the United States and Soultz in France have verified the technical feasibility of EGS [7]. However, practical experience has also shown that conventional multi-well EGS systems face challenges, including high drilling costs, large upfront investment, strong sensitivity to well spacing design, and a high risk of thermal breakthrough, which severely constrain their large-scale commercial deployment [8].

To reduce development costs and enhance system flexibility, various

* Corresponding author.
E-mail address: g.song-1@tudelft.nl (G. Song).

https://doi.org/10.1016/j.renene.2026.126549
Received 26 March 2026; Received in revised form 8 October 2026; Accepted 8 October 2026
Available online 9 October 2026
0960-1481/© 2026 The Authors. Published by Elsevier Ltd. This is an open access article under the CC BY license (http://creativecommons.org/licenses/by/4.0/).



(a) 3D schematic diagram for the field implementation (b)Top view (c) Section view

Fig. 1. Schematic diagram for MCML-EGS. Three casings correspond to connected three-layer multilateral wells inside. The mid-layer multilateral wells are for injection, and upper- and lower-layer multilateral wells are for production.

open-loop coaxial well EGS configurations have been proposed and investigated in recent years [9,10]. Such systems typically drill only one main well and achieve injection and production cycles through concentric pipe structures, wellbore zonal isolation, or lateral branch wells, which significantly reduces the number of wells drilled and engineering investment. Among these designs, the open-loop coaxial well Enhanced Geothermal System realizes the injection-production circulation through the annulus between inner and outer pipes, which lowers development costs and improves system controllability [11,12]. In contrast, the single-casing coaxial well EGS with multilateral branches (ML-EGS) increases the contact area between the wellbore and the reservoir fracture network by drilling multiple horizontal lateral branches from the main wellbore, thereby improving reservoir heat extraction and heat exchange efficiency [10,13]. Limited by the number of wellbores and spatial configuration, a single coaxial well can only stimulate a local portion of the reservoir, resulting in a limited heat-transfer area and constraining long-term heat extraction performance [14]. Therefore, how to enlarge the effective reservoir stimulation volume and improve heat-exchange efficiency while retaining the low-cost advantage of a single-main-well configuration remains a key challenge for current single-well EGS technologies.

In this work, we propose a previously unreported Enhanced Geothermal System based on a coaxial well configuration featuring multiple casings and multilateral branches (MCML-EGS), as illustrated in Fig. 1(a). The system comprises a single main vertical well, from which lateral branches are created in the upper, middle, and lower sections of the reservoir using microhole coiled-tubing (CT) drilling technology. Hydraulic fracturing is then applied to activate and expand the natural fracture network, forming a stimulated reservoir zone that connects the lateral branches across these sections. A multi-layer casing assembly, consisting of an inner pipe and an annular pipe, is subsequently installed within the wellbore as shown in Fig. 1(b). Packers are positioned between the wellbore casing and the annular pipe, and between the annular pipe and the inner pipe, thereby dividing the main well into one injection zone and two production zones (upper and lower), as illustrated in Fig. 1(c). This configuration establishes multiple heat exchange regions between the injection zone and the two production zones, enabling the working fluid to undergo heat exchange over a substantially larger reservoir volume. Compared with conventional single-coaxial-well EGS configurations, the proposed system achieves a larger stimulated reservoir volume and a greater effective heat exchange area without requiring additional main wells. Furthermore, the multi-casing coaxial configuration spatially separates the injection and production pathways, which reduces excessive concentration of flow within a single channel and promotes a more uniform fluid distribution throughout the fracture network. This configuration is expected to reduce the injection-production pressure difference, decrease circulating-pump energy consumption, and improve the overall energy efficiency of the system. However, research on multi-casing coaxial EGS configurations remains limited, and their fluid-flow characteristics and heat transfer mechanisms have not yet been systematically understood.

Given the high cost and difficulty of field experiments in hot dry rock, numerical simulation offers an efficient way to study heat extraction performance in fractured reservoirs. Liao et al. [15] studied the influence of fracture evolution on the long-term heat recovery performance of EGS based on the DFN-THM coupling model and found that fracture connectivity plays a decisive role in thermal breakthrough time and pressure response. Song et al. [16] investigated the fracture aperture evolution for EGS based on a thermo-hydro-mechanical-chemical fully coupled model and then evaluated the contributions of different coupling effects to the variation of reservoir properties and production dynamics. Zhang et al. [17] studied the potential of multibranch well structures in fractured geothermal reservoirs and found that multi-branch wells can improve the initial heat recovery capacity, but the efficiency is limited in highly fractured reservoirs. Hou et al. [18] pointed out that in fracture-intensive reservoirs, thermal short-circuit is more likely to occur in horizontal wells or multi-well systems, affecting long-term thermal stability. Previous research on multilateral wells provides valuable guidance for this study and informs the proposed system design. In addition, sensitivity analyses of MCML-EGS heat extraction performance remain limited.

This study introduces a multi-casing coaxial well with multilateral branches (MCML-EGS) and establishes a three-dimensional fully coupled thermo-hydro-mechanical (THM) model with discrete fracture networks (DFNs) to analyze the heat extraction performance of MCML-EGS. First, the coupled flow and heat-transfer behavior of the MCML-EGS in reservoir fractures is evaluated by analyzing temperature, seepage velocity, pressure, and stress fields. Second, the MCML-EGS is compared with the conventional single-casing multilateral-well system to evaluate differences in outlet temperature, cumulative energy production and pressure difference. Then, the effects of key factors (fracture number, branch-well number and length, and injection rate) on system heat transfer, energy production, and pressure response are analyzed. Finally, the preliminary economic and engineering feasibility is assessed, and the system's life-cycle potential for efficient, stable, and low-cost heat recovery is evaluated. The results are expected to provide theoretical and engineering references for hot dry rock EGS design and parameter optimization.

2. Mathematical models and simulation settings for the MCML-EGS

2.1. Model assumptions

The fundamental assumptions listed below are adopted in establishing the three-dimensional numerical model for the MCML-EGS.

(1) The hot dry rock reservoir matrix is treated as an isotropic and continuous poroelastic medium [19,20].
(2) Fractures are explicitly represented as high-permeability fluid-flow pathways using the discrete fracture network (DFN) approach. The fracture dip angle, (θ), and fracture length, (L), are treated as random variables satisfying ($\theta \sim U([0^\circ, 30^\circ] \cup [60^\circ, 120^\circ])$) and ($L \sim U(50, 300)$ m), respectively, within the prescribed parameter ranges [21,22]. The spatial orientation of each branch is defined in the global coordinate system by its inclination angle and azimuth angle, which characterize its deviation from the vertical direction and its horizontal orientation, respectively.
(3) Water is modeled as a single-phase fluid with temperature-dependent properties, while phase change and chemical effects are neglected [23].
(4) Fluid flow in both the porous matrix and fractures is assumed to obey Darcy's law, and non-Darcy flow behavior and inertial effects that may arise under high-velocity conditions are neglected [22,24].
(5) Heat transfer includes convection between fluid and rock and conduction through the rock. The matrix is assumed to be in local thermal equilibrium without fluid convection, and fracture-rock heat exchange is modeled using a local thermal equilibrium model [25].
(6) The main wellbore is fully isolated, preventing short-circuiting, and heat transfer through the casing is neglected.
(7) Rock deformation follows linear elasticity, accounting for temperature and pore pressure effects, while ignoring failure, plasticity, and creep [26].

2.2. Governing equations

The partial differential equation of rock deformation can be written in the following form, taking into account how temperature and pore pressure affect rock stress [27]:

$$\frac{E}{2(1+\nu)}u_{i,jj} + \frac{E}{2(1+\nu)(1-2\nu)}u_{j,ji} - a_B p_{,i} - a_T \frac{E}{(1-2\nu)}T_{s,i} + F_i = 0 \quad (5)$$

where E is the elastic modulus, GPa; ν is the Poisson ratio; u_i is the displacement, m; α_B is the Biot coefficient; p is the pore pressure, Pa; $T_{s,i}$ is the temperature gradient in the i-th direction (K/m); F is the body force per unit volume, N/m^3; α_T is the coefficient of thermal expansion, 1/K.

The stress-displacement relationship for fractures is:

$$u_n = \frac{\sigma_n}{K_n} \quad (6)$$

where u_n is the normal displacement of the fracture, m; K_n is the normal stiffness, Pa/m; σ_n is the corresponding normal stress, Pa. Fluid flow in the porous matrix is described by Darcy's law, and the governing equation is [28]:

$$\rho_f S_s \frac{\partial p}{\partial t} + \rho_f \nabla \cdot \mathbf{v} = -\rho_f \frac{\partial \varepsilon_s}{\partial t} \quad (7)$$

$$\mathbf{v} = -\frac{k_s}{\eta}\nabla p \quad (8)$$

where. ρ_f.is the density of working fluid, kg/m^3; S_s is the storage coefficient of the HDR matrix, 1/Pa. p is the matrix pore pressure, Pa; ε_s is the volumetric strain; $\mathbf{v}$ is the seepage velocity, m/s; k_s is the permeability of the matrix, m^2; η is the dynamic viscosity of the working fluid, Pa·s. Fluid flow in discrete fractures can be characterized as [28]:

$$\rho_f e_h S_f \frac{\partial p}{\partial t} + \nabla \cdot (\rho_f e_h \mathbf{v}_f) + \rho_f \frac{k_f}{\eta}\frac{\partial p}{\partial n} = -\rho_f e_h \frac{\partial \varepsilon_f}{\partial t} \quad (9)$$

$$\mathbf{v}_f = -\frac{k_f}{\eta}\nabla p \quad (10)$$

$$k_f = \frac{(d_0 - u_n)^2}{12} \quad (11)$$

where e_h is the fracture aperture; S_f is the storage coefficient of fracture, 1/Pa; k_f is the permeability of fracture, m^2; ε_f is the volumetric strain of the fracture, and d_0 is the initial fracture aperture, m.

A local thermal equilibrium model is used in the study to represent the heat exchange between fluid and rock. Therefore, the energy conservation equation can be used to describe heat transfer in the rock as follows [29]:

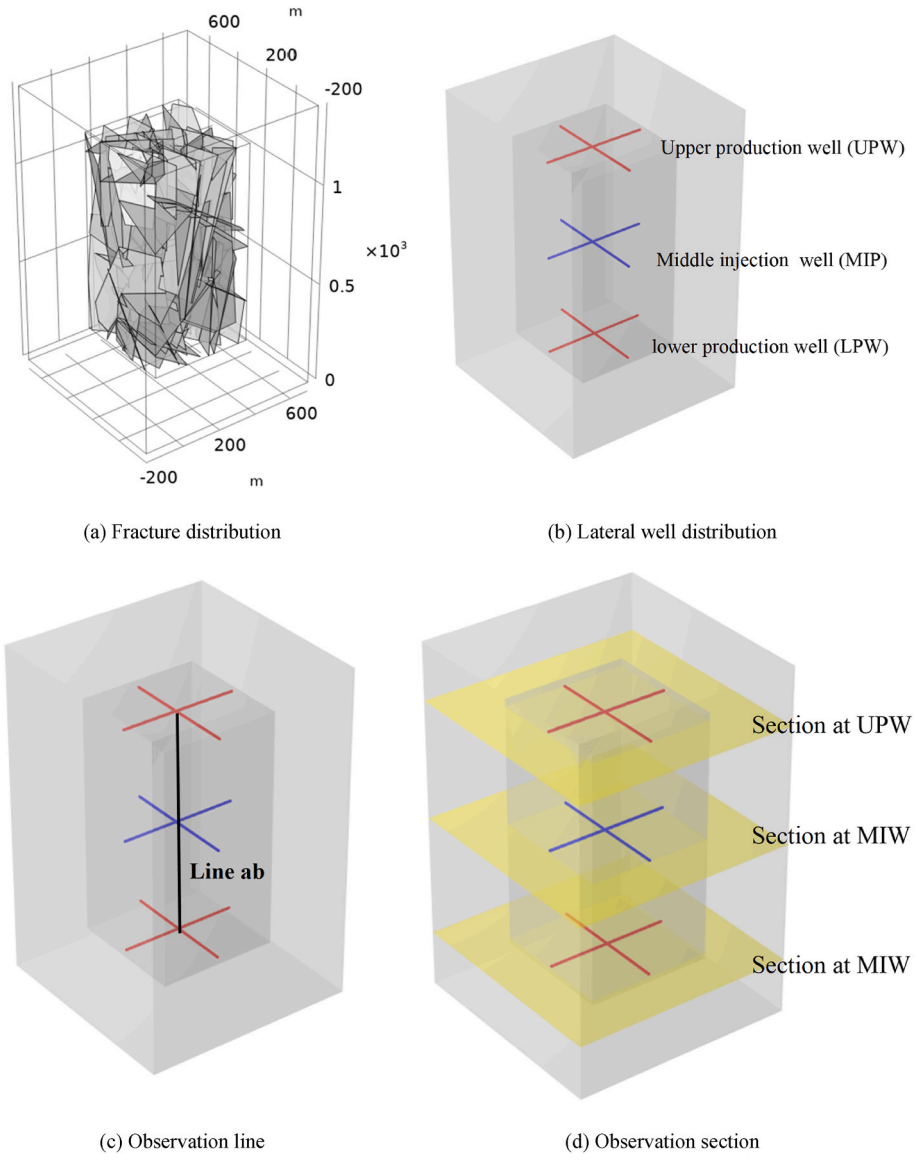
$$(\rho c)_{eff}\frac{\partial T_s}{\partial T} + \rho_f c_f \mathbf{v} \cdot \nabla T_s - \lambda_{eff}\nabla^2 T_s = -Q_{fE} \quad (12)$$

$$\rho_f = \begin{cases} 1000 \times \left(1 - \dfrac{(T_f - 3.98)^2}{503570} \times \dfrac{T_f + 283}{T_f + 67.26}\right) & 273.15 \le T_f < 298.15\text{K} \\ 996.9 \times (1 - 3.17 \times 10^{-4})(T_f - 25) - 2.56 \times 10^{-6}(T_f - 25)^2) & 298.15 \le T_f < 523.15\text{K} \\ 1758.4 + 10^{-3}T_f(-4.8434 \times 10^{-5} + T_f(1.0907 \times 10^{-5} - 9.8467 \times 10^{-9}T_f)) & 523.15 \le T_f < 753.15\text{K} \end{cases} \quad (1)$$

$$\mu_f = \begin{cases} 10^{-3} \times (1 + 0.015512(T_f - 20)) & 273.15 \le T_f < 37.315\text{K} \\ 0.2414 \times 10^{-3} \times 10^{\left(\frac{247.8}{T_f + 133.15}\right)} & 373.15 \le T_f < 573.15\text{K} \end{cases} \quad (2)$$

$$c_f = 12010.1 - 80.4T_f + 0.3T_f^2 - 5.4 \times 10^{-4}T_f^3 + 3.6 \times 10^{-7}T \quad 273.1K \le T_f < 573.15K \quad (3)$$

$$\lambda_f = -0.8691 + 0.0089T_f - 1.5837 \times 10^{-5}T_f^2 + 7.9754 \times 10^{-9}T \quad 273.1K \le T_f < 573.15K \quad (4)$$



(a) Fracture distribution (b) Lateral well distribution

(c) Observation line (d) Observation section

Fig. 2. Geometric model for base case with 150 fractures and four lateral wells.

$$(\rho c)_{eff} = (1-\varphi)\rho_s c_s + \varphi\rho_f c_f \tag{13}$$

$$\lambda_{eff} = (1-\varphi)\lambda_s + \varphi\lambda_f \tag{14}$$

where T_s is the temperature of the HDR matrix, °C; $(\rho c)_{eff}$ and λ_{eff} are effective volumetric heat capacity (J/(m^3·K)) and effective thermal conductivity (W/(m·K)), respectively. φ is the porosity of the matrix; ρ_s is the density of the matrix, kg/m^3, c_s is the specific heat capacity of the matrix, J/(kg·K); ρ_f is the density of fluid, kg/m^3; c_f is the specific heat capacity of the working fluid, J/(kg·K). λ_s is the thermal conductivity of the matrix, W/(m·K); λ_f is the thermal conductivity of the working fluid, W/(m·K). Q_{fE} is the volumetric heat exchange term between the fracture fluid and the rock matrix, W/m^3. Energy conservation in the fracture is expressed as:

$$\rho_f c_f \frac{\partial T_f}{\partial t} + \rho_f c_f \nabla \cdot (\mathbf{v}_f T_f) - \nabla(\lambda_f \nabla T_f) = Q_{fE} \tag{15}$$

where λ_f is the thermal conductivity of the working fluid, W/(m·K). The THM model validation against the analytical models can be found in the **Appendix**.

2.3. Evaluation metrics

2.3.1. Technological metrics

The production temperature of the MCML system can be defined as the average temperature of the fluid produced by the production well:

$$T_{pro} = \frac{\int_L T(l,t)dl}{L} \tag{16}$$

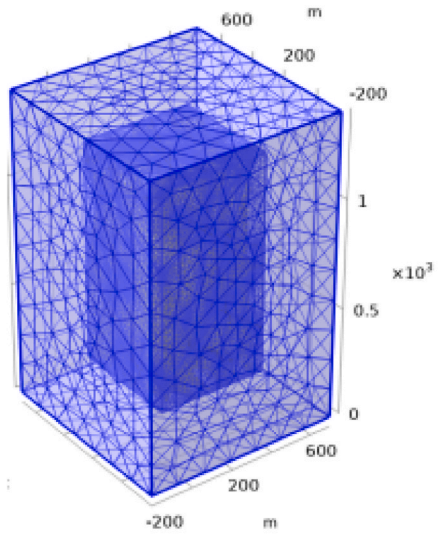
where L is the overall length of the production well, m; $T(l, t)$ is the production temperature at position l along the production well at time t, K. The thermal production power is defined by

$$W_{pro} = c_w q(T_{pro} - T_{in}) \tag{17}$$

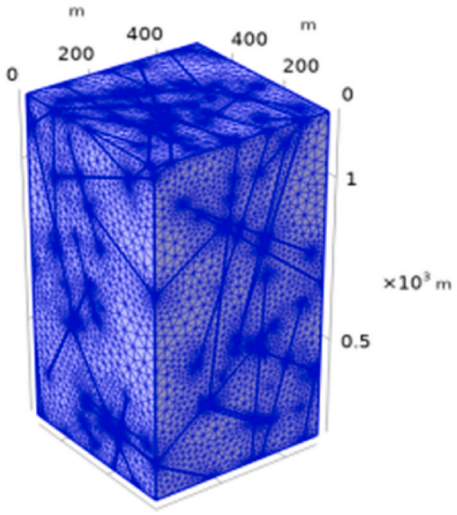
where T_{in} is the injection temperature, K; q is the overall mass flow rate throughout the process of heat extraction, kg/s; c_w is the specific heat capacity of the fluid, J/(kg·K). The cumulative production thermal energy (J) is defined as follows:

$$E_{pro} = \int c_w q(T_{pro} - T_{in})dt \tag{18}$$

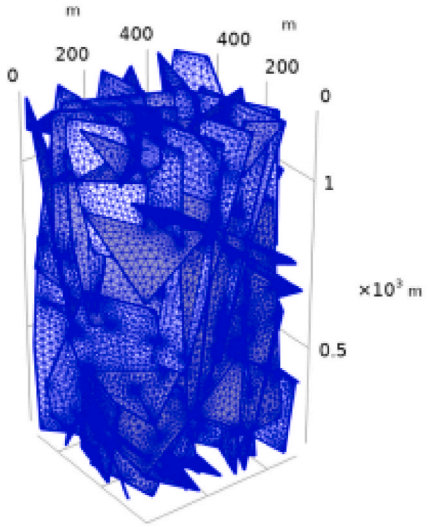
The pump power (W) and pump energy consumption (J) are



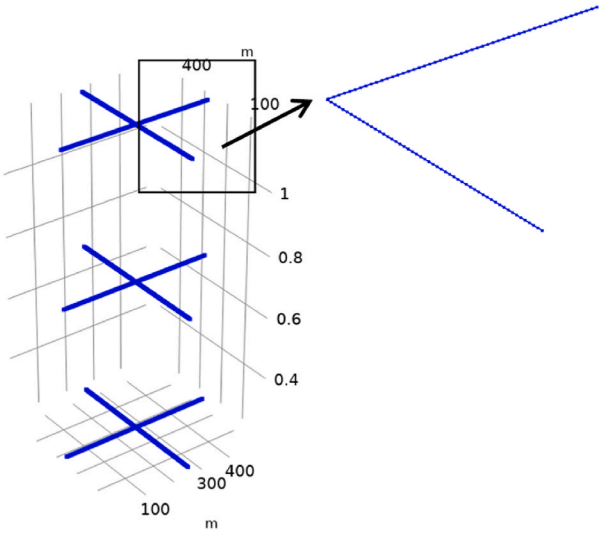
(a) Mesh for the whole reservoir



(b) Refinement for the SRV



(c) Mesh for fractures



(d) Mesh for wells

Fig. 3. Mesh for the base case with 150 fractures, four lateral wells, and an injection rate of 60 kg/s.

described as [30,31]:

$$W_{pump} = \frac{q(p_{in} - \rho_f g h_{in})}{\rho_w \eta_{pump}} + \frac{q\left(\rho_f g h_{pro} - p_{pro}\right)}{\rho_w \eta_{pump}} \tag{19}$$

$$E_{pump} = \int W_{pump} dt \tag{20}$$

where p_{in} is the injection pressure, Pa; p_{pro} is the production pressure, Pa; h_{in} and h_{pro} are the depths of injection and production wells, m; η_{pump} is the pump efficiency.

2.3.2. Economic metrics

The cost of geothermal systems (C_{total}, M$) consists of two parts: surface costs (C_{surf}, M$) and subsurface costs ($C_{sub}$, M$).

$$C_{total} = C_{surf} + C_{sub} \tag{21}$$

Usually, subsurface costs include drilling costs and fracturing costs, among which drilling costs can be calculated using the following formula [29,32]:

$$C_{drill} = \left(600 H_{mv} + 1500 H_{ph}\right) \times 10^{-6} \tag{22}$$

where C_{drill} is the drilling cost, M$; H_{mv} is the length of the main vertical well, m; 600 is the drilling cost of the main horizontal well per length, $/m; H_{mh} is the length of the lateral well, m; 1500 is the drilling cost of the lateral well per length, $/m. The installation cost of ground equipment is closely associated with the power generation of geothermal systems, and the unit installation cost of power generation equipment ($/MW) can be expressed as follows [32]:

$$U_{ei} = 2 \times 10^6 \times \mathbf{exp}(-0.0045 \times (P - 5)) \tag{23}$$

where P is the generated thermal power, MW. The total cost of installing a geothermal power generation system (M$) can be expressed as follows:

$$C_{ei} = 4.3 + \frac{U_{ei} \times P}{10^6} \tag{24}$$

The unit ($/MWh) and total (M$) operating and maintenance costs of a geothermal system can be expressed as follows [32]:

$$U_{om} = 20 \times \mathbf{exp}(-0.0025 \times (P-5)) \tag{25}$$

$$C_{om} = U_{om} \times E_{pro} \times 10^{-6} \tag{26}$$

The cost of hydraulic fracturing is also a component of the cost of geothermal systems. According to the literature, the cost of hydraulic fracturing is 0.95, 1.87, 2.74 and 3.74 M$ for 50, 100, 150, and 200 hydraulic fractures, respectively [22,33]. The total cost of the system can be calculated using the following formula:

$$C_{total} = C_{surf} + C_{sub} = C_{ei} + C_{om} + C_{fra} + C_{drill} \tag{27}$$

The levelized cost of energy (LCOE) can be calculated using the following formula:

$$C_{unit} = \frac{C_{total}}{E_{pro} - E_{pump}} \tag{28}$$

2.4. Geometric model

The reservoir geometry and physical properties for MCML-EGS are modeled using parameters from existing numerical studies in typical EGS projects. As shown in Fig. 2(a), the computational model consists of the reservoir stimulation volume (i.e., the hydraulic fracturing activation zone) and its surrounding rock. The reservoir stimulation volume measures 500 m × 500 m × 1000 m. The fracture dip angles are randomly generated within the ranges of 0-30° and 60-120°. Fracture lengths are randomly generated from 50 m to 300 m. The number of fractures in the base case is 150. The surrounding rock extends 200 m outward from each side of the stimulation volume, forming a three-dimensional computational domain of 900 m × 900 m × 1400 m. The spatial arrangement of the injection and production branches is shown in Fig. 2(b): the central area is set as the injection well section, with upper and lower production wells arranged 500 m above and below it, respectively. This configuration enables coordinated development of the upper and lower parts of the reservoir.

To analyze the change of the reservoir temperature field more clearly, we set the observation line ab in the geometric model, as shown in Fig. 2(c). An observation section is set up at the middle injection well and the upper and lower production wells, as shown in Fig. 2(d), and the temperature variations at the three wells are analyzed.

2.5. Initial and boundary conditions

For static stress equilibrium, the model is buried at a depth of 3800 m, with an in-situ stress gradient set at 25 MPa/km. Accordingly, a load of 95 MPa is applied to the top boundary, while the bottom boundary is assigned a fixed (roller) support. The surrounding lateral boundaries are prescribed as stress boundaries:

$$\sigma_x = \sigma_y = 95 + \gamma z \tag{29}$$

where σ_x and σ_y are stress along the x and y directions, respectively. For the heat transfer, the initial temperature is determined by applying a geothermal gradient of 0.05 °C/m, expressed as:

$$T = T_0 + \nabla T \cdot Z \tag{30}$$

where T_0 is the surface temperature, °C, Z denotes depth, m, and ∇T represents the geothermal gradient, set to 0.05 °C/m. Heat exchange between the model boundaries and the model interior follows:

$$n \cdot q = h(T_{ext} - T) \tag{31}$$

Within the EGS configuration, fluid is injected at 20 °C, while the production well temperature is treated as a free boundary. The initial pressure distribution is dominated by the hydrostatic pressure gradient of 9.81 MPa/km. The reservoir pressure is calculated using:

$$p = 39.2 + \nabla p \cdot Z \tag{32}$$

The injection flow rate of the MCML-EGS system is set to 60 kg/s.

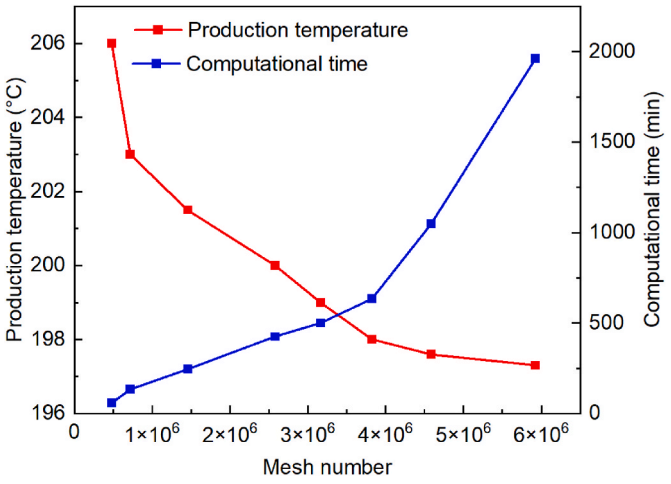


Fig. 4. Production temperature at Year 30 and corresponding computational time for different numbers of mesh elements.

Table 1
Mesh refinement results in terms of production temperature, computational time, and GCI [3].

Mesh type	Number of mesh elements	Production temperature (°C)	Computational time (min)	Grid Convergence Index (%)
Coarse	1458790	201.5	245	-
Medium	3825821	198	635	0.48
Fine	5921553	197.3	1960	0.30

2.6. Simulation mesh

Fig. 3 illustrates the mesh generation for the base case of ML-EGS and MCML-EGS. Based on different physical processes and geometric features, the mesh system for the computational domain can be categorized into three types: 3D mesh for the hot dry rock reservoir matrix, 2D mesh for the fractures, and 1D mesh for the lateral wells. Specifically, the hot dry rock reservoir matrix is discretized using free tetrahedral elements, as shown in Fig. 3(a). Given that fluid-flow and heat-transfer processes occur primarily in the stimulated reservoir volume (SRV) region, local mesh refinement is performed to enhance the precision of the numerical simulation, as shown in Fig. 3(b). In contrast, relatively coarse meshing is used in the surrounding rock region to reduce the overall computational load while maintaining computational accuracy. To further improve computational efficiency, the fracture network is discretized using two-dimensional elements, while the branch wells are modeled using one-dimensional elements, as shown in Fig. 3(c) and (d), respectively.

A mesh-independence analysis was conducted to identify an appropriate number of mesh elements while maintaining computational efficiency. The variation in the production temperature at Year 30 with the number of mesh elements is presented in Fig. 4. The predicted production temperature exhibits progressively smaller variations as the number of mesh elements increases beyond 3.82 million, while the computational time increases significantly. To further quantify the discretization uncertainty, the Grid Convergence Index (GCI) was employed [3]. The GCI for the selected mesh containing 3.82 million elements is 0.48%,

Table 2
Parameters used in the numerical simulation of MCML-EGS.

Component	Density (kg/m^3)	Porosity	Thermal conductivity (W/(m·K))	Specific heat capacity (J/(kg·K))	permeability (m^2)	E(GPa)	v	a_T
Rock matrix	2800	0.05	2.8	800	10^{-18}	30	0.2	5×10^{-6}
Fracture	1200	1	1	1200	$d_0=0.001$m	-	-	-

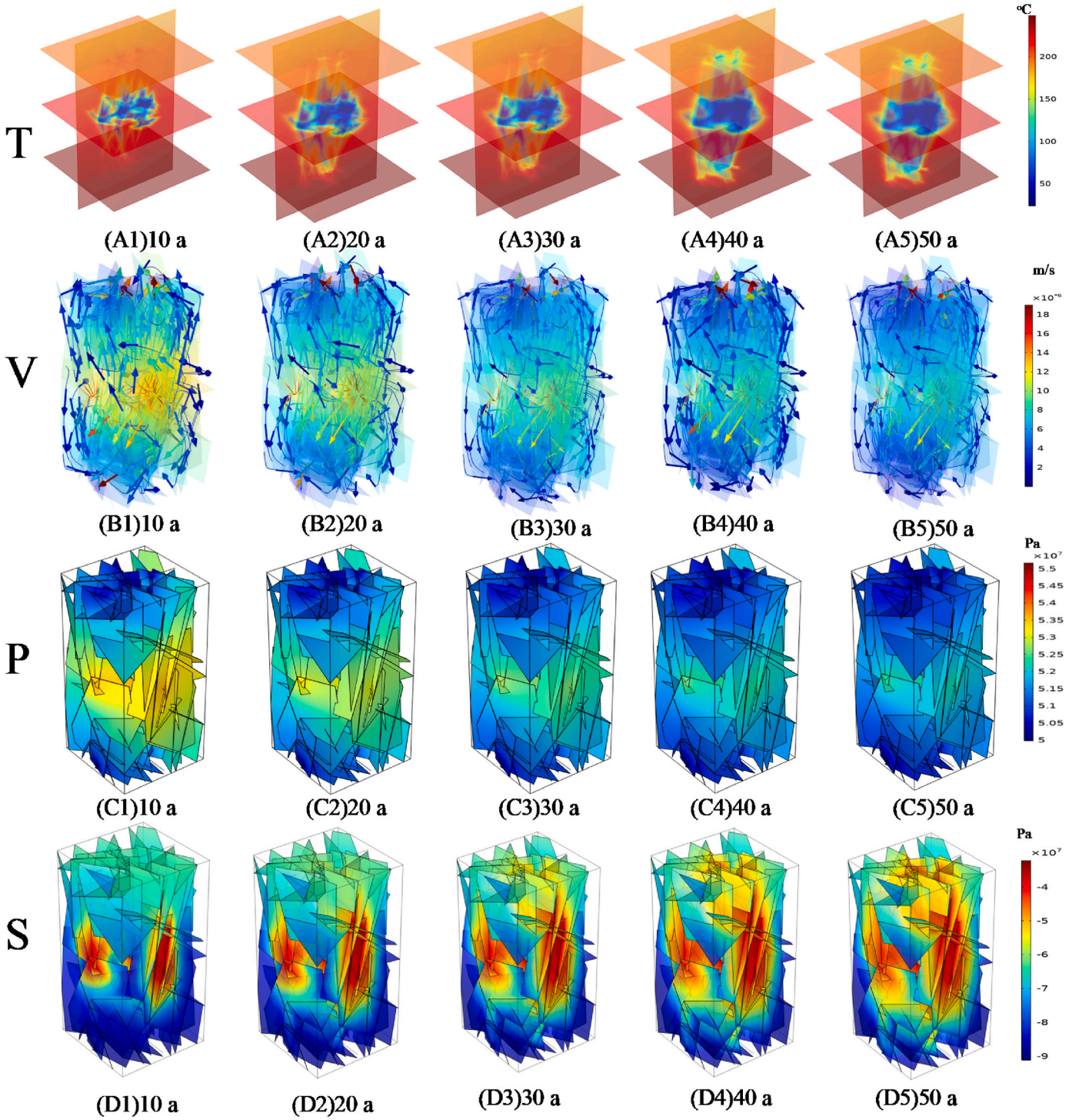
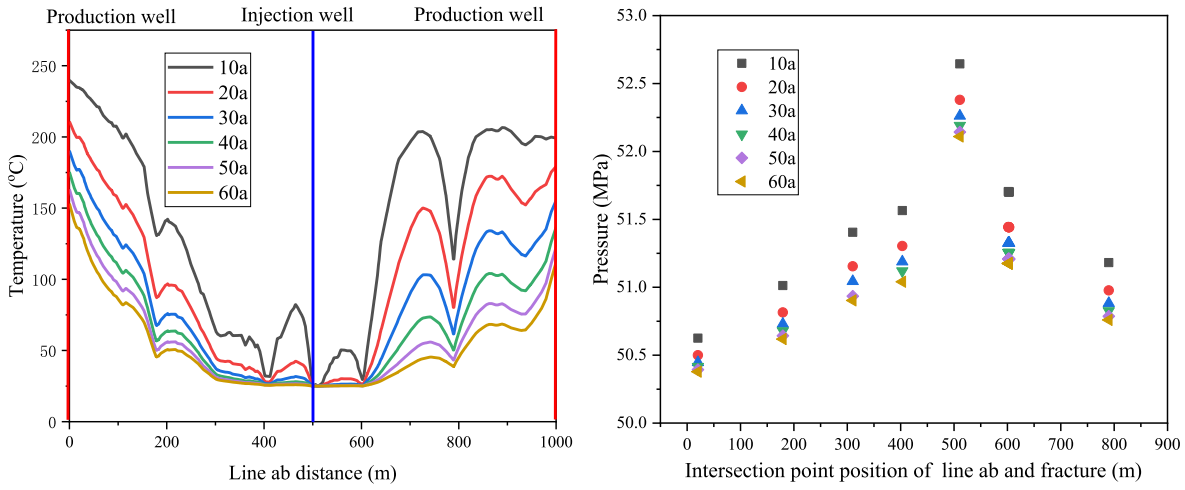


Fig. 5. Temperature, Flow Velocity, and Pressure for the Base Case. T: temperature, °C; V: velocity, m/s; P: pressure, Pa; S: effective stress, Pa.

indicating a relatively small discretization uncertainty (see Table 1). Further refinement to 5.92 million elements changes the Year-30 production temperature by only 0.7 °C, which does not affect the conclusions of the comparative analysis. Therefore, considering both numerical accuracy and computational efficiency, a mesh containing approximately 3.82 million elements was adopted for the subsequent



(a) Temperature along the line ab

(b) Pressure at the intersection points of the observation line ab and the fractures

Fig. 6. Temperature and pressure along the observation line (q = 60 kg/s).

simulations. The simulations are conducted using the property parameters listed in Table 2.

3. Results

3.1. Multiphysics fields

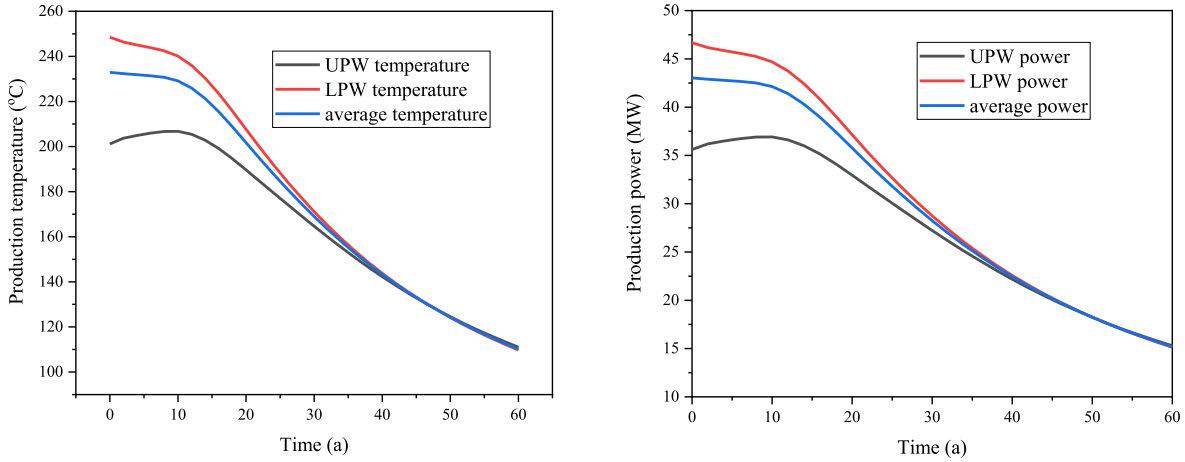
Fig. 5 (A1-A5) displays the distribution of the temperature field at different production times. In the initial phase of production (10 years), the low-temperature zone is mainly distributed on both sides of the middle injection well; as injection time increases, the low-temperature zone gradually expands toward the upper and lower production wells and covers most of the reservoir area after 50 years of production. This shows that the MCML-EGS can effectively utilize a reservoir volume of approximately 500 m × 500 m × 1000 m, thereby significantly improving the extraction rate of reservoir thermal energy.

Fig. 5 (B1-B5) shows the variation of velocity with time. The high-velocity region is mainly within the stimulated reservoir volume, and the flow rate decreases with heat extraction time. This is primarily due to the temperature decrease along the reservoir fracture surfaces, the increase in fracture aperture, and the gradual development of seepage channels, which reduce fluid resistance.

Correspondingly, as the reservoir seepage resistance decreases, the pressure difference between the injection well and the production well gradually decreases with heat-extraction time, as shown in Fig. 5 (C1-C5). The results show that the MCML-EGS not only maintains a large effective volume for heat transfer during long-term operation, but also helps reduce the pressure difference, thereby improving the energy efficiency of the system.

Fig. 5 (D1–D5) shows effective stress changes over time. Early in heat extraction, high-pressure cold water creates a low-temperature zone near the injection well, forming a low-stress area around 32 MPa in the middle of the reservoir, while uncooled regions remain at about 90 MPa. Over time, the low-stress zone expands toward the production wells, reducing reservoir resistance and promoting fluid flow.

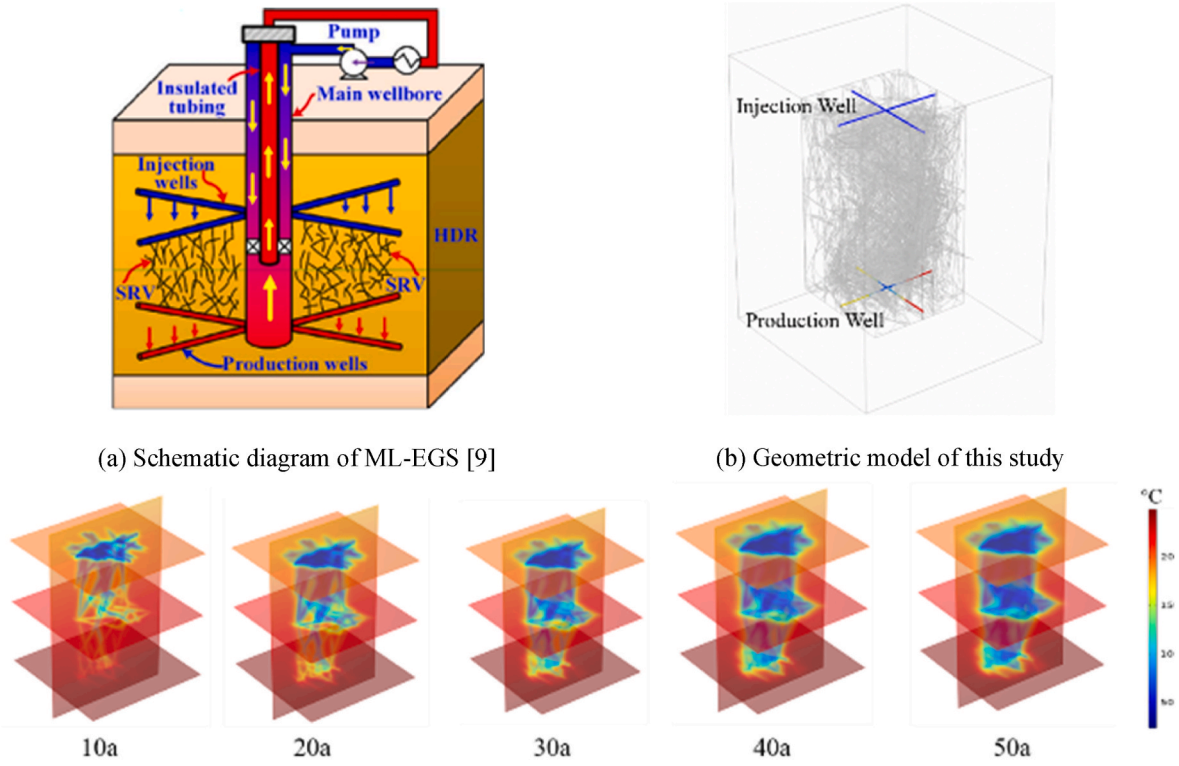
In general, the temperature, flow-rate, pressure, and effective-stress fields all show a highly coupled evolution trend: the middle injection well provides hydraulic displacement, while the upper and lower production wells form a low-pressure area, which diverts the injected fluid to multiple flow paths; this three-layer layout structure can expand the



(a) Production temperature

(b) Production power

Fig. 7. Production temperature and production power.



(a) Schematic diagram of ML-EGS [9]

(b) Geometric model of this study

(c) Temperature distribution of the ML-EGS (q = 60 kg/s)

Fig. 8. Schematic diagram for ML-EGS in (a) and (b); temperature distribution of ML-EGS (q = 60 kg/s) in (c).

vertically affected reservoir volume, and the pressure-stress response can enhance the connectivity of the fracture network. As a result, the injected fluid is distributed more widely throughout the reservoir, dominant high-velocity channels are weakened, and the fluid is dispersed toward the production wells. This mechanism can increase the contact area and residence time between the fluid and the rock matrix, thus helping to delay the cold front propagation. Previous open-loop geothermal systems based on single coaxial wells or limited multilateral configurations mainly access relatively localized reservoir volumes due to the limited heat exchange area. Song et al. [10] and Gao et al. [34] improved heat extraction by optimizing multilateral wells. Here, the proposed MCML-EGS further expands the heat exchange volume through a three-layer coaxial structure with upper and lower production branches.

To better illustrate fluid flow and heat transfer from the middle injection well to the upper and lower production wells, line ab is used to show temperature and pressure distributions (Fig. 6). The injection well has the lowest temperature, as shown in Fig. 6(a). As fluid flows toward both production wells, temperature increases with fluctuations due to different heat transfer mechanisms: strong convective cooling in fractures and slower conductive heat transfer in the rock matrix. Over time, reservoirs on both sides of the injection well are gradually cooled. After 10 years, the lower production well region remains hotter than the upper region, while by 50 years, temperatures become nearly uniform, indicating balanced heat extraction. Fig. 6(b) presents pore pressure along the same line. Due to the low permeability of the HDR matrix, only fracture intersections are considered, resulting in discrete pressure points. Spatially, pressure is highest at the injection well and decreases toward the production wells. Temporally, reservoir pressure first rises and then declines, reflecting improved seepage conditions during long-term operation.

Fig. 7 shows the temporal variations in reservoir outlet temperature and production power. As shown in Fig. 7(a), in the early stage of thermal recovery, the temperature of the lower production well is higher than that of the upper production well; this is because the initial temperature of the lower part of the reservoir is higher than that of the upper part, so that the lower production well can extract more heat. Subsequently, the reservoir temperature decreased steadily with time, and the temperatures of the upper and lower production wells gradually converged. Fig. 7(b) shows the variation of system power generation with time, and its trend is broadly consistent with the temperature trend: during the period from year 0 to year 60, the average power generation decreased from 42 MW to 15 MW.

3.2. Comparative analysis

This subsection compares the differences between the MCML-EGS and ML-EGS in terms of heat extraction efficiency. The single-well MCML-EGS places the injection well at the reservoir center and production wells at both ends, as shown in Fig. 2. In contrast, ML-EGS (Fig. 8(a) and (b)) separates injection and production using a single casing, with injection typically in the upper reservoir and production in the lower part.

Fig. 8(c) shows the temperature distribution for ML-EGS. With the same injection rate of 60 kg/s for both systems, the low-temperature region in the ML-EGS is larger than that in the MCML-EGS (Fig. 5 (A1-A5)) by the 10th year, indicating that thermal breakthrough occurs earlier in the ML-EGS. The low-temperature zone in ML-EGS becomes more pronounced with time, adversely affecting the long-term geothermal potential of the reservoir.

Fig. 9 presents a comparative analysis of the reservoir production temperature, production power, and pressure difference between MCML-EGS and ML-EGS. As shown in Fig. 9(a), the average outlet temperature of the MCML-EGS is significantly higher than that of the ML-EGS throughout the entire operational period. Following 30 years of heat extraction, the mean outlet temperature of the MCML-EGS was

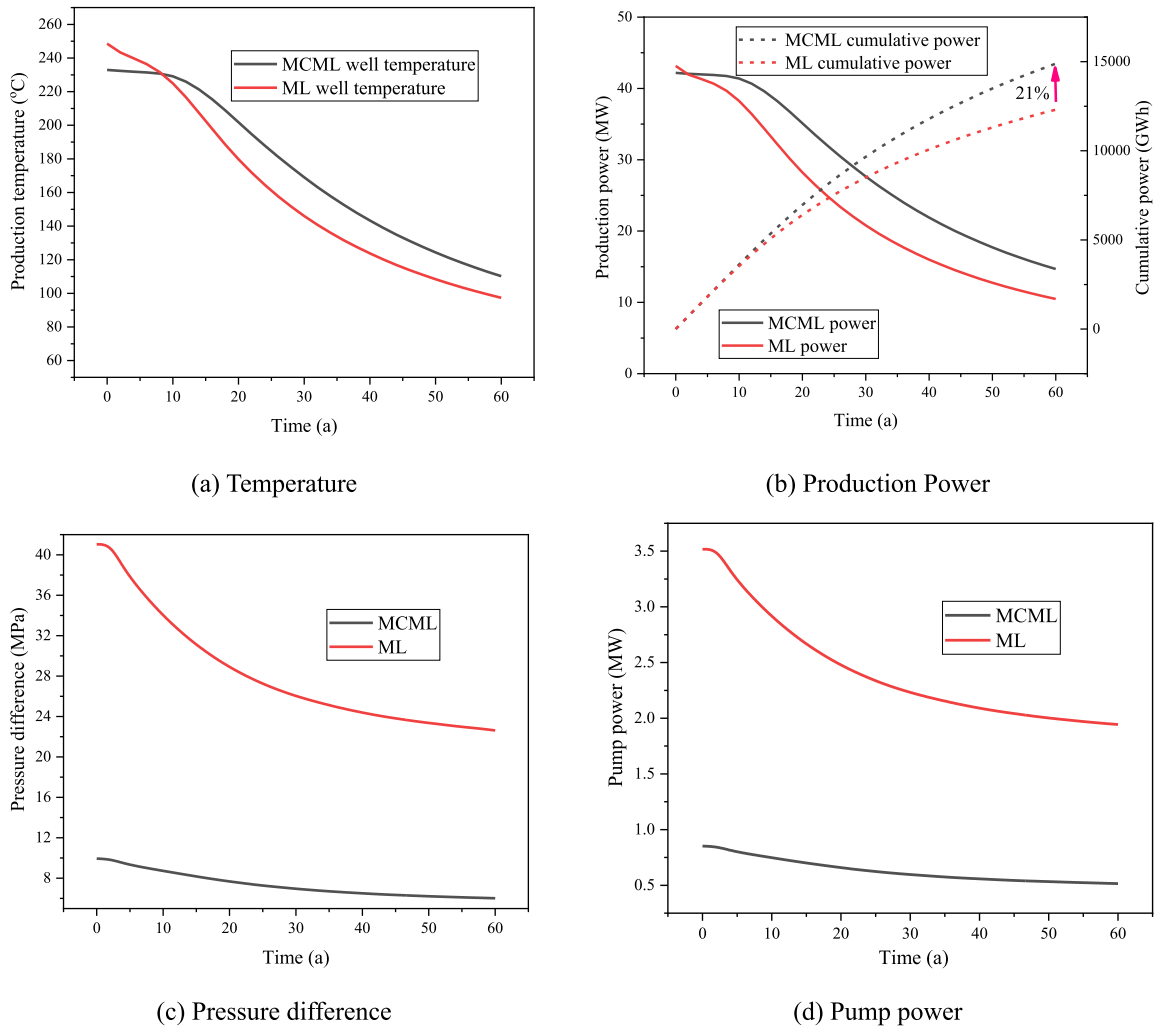


Fig. 9. Comparison of (a) production temperature, (b) production power, (c) pressure difference, and (d) pump power for MCML-EGS and ML-EGS (q = 60 kg/s).

approximately 168 °C, while that of the ML-EGS was only about 146 °C. After 60 years of heat extraction, the production temperature of the MCML-EGS remained at approximately 110 °C, while that of the ML-EGS had dropped to approximately 97 °C, indicating that the MCML-EGS has better thermal stability during long-term operation.

Fig. 9(b) shows the variation of the production power of the two systems with time. The MCML-EGS maintains a higher power level throughout the production period. At the end of the 60-year production period, the cumulative energy production of the MCML-EGS is about 14,884 GWh, while that of the ML-EGS is about 12,305 GWh, and the former is about 21% higher than the latter. MCML-EGS can significantly improve the overall recovery efficiency of reservoir thermal energy without increasing the number of main wells and with only a limited increase in drilling costs.

Fig. 9(c) and (d) show the pressure difference between the injection well and the production well and the energy required to pump the fluid, respectively. The maximum pressure difference of the MCML-EGS system is 4.9 MPa, while the maximum pressure difference of the ML-EGS system is 41.5 MPa. The maximum pumping power of the MCML-EGS system is 0.08 MW, while the maximum pumping power of the ML-EGS is up to 3.5 MW. Overall, the MCML-EGS requires substantially less pumping power at the same injection flow rate.

3.3. Parametric analysis

3.3.1. Fracture number

Increasing fractures enhances reservoir permeability and heat transfer area, but excessive or uneven fractures can cause short-circuiting and reduce heat exchange. This section simulates MCML-EGS performance with 50, 100, 150, 200, and 250 fractures.

Fig. 10 illustrates the variation of the reservoir temperature field with the fracture number at different injection times. The three-dimensional diagram shows the temperature distribution on the hydraulic fracture surface, with the upper, middle, and lower sections representing the upper production well section, the middle injection well section, and the lower production well section (Fig. 2(d)). Taking 30 years as an example, the temperatures of the top and bottom sections decrease when there are 50 and 100 fractures (Fig. 10(a and b)). The low-temperature zone in the middle injection well section gradually decreases with the number of fractures. When the number of fractures is over 150, the area of the low-temperature region in the middle injection well section no longer varies significantly, as shown in Fig. 10(c–e). This shows that the MCML system can effectively extract reservoir heat under different fracture numbers, and the extraction efficiency increases with the number of fractures. However, when the number of fractures exceeds a certain threshold, the increase in extraction efficiency is no longer significant.

Fig. 11 and Table 3 present the production capacity of reservoirs with

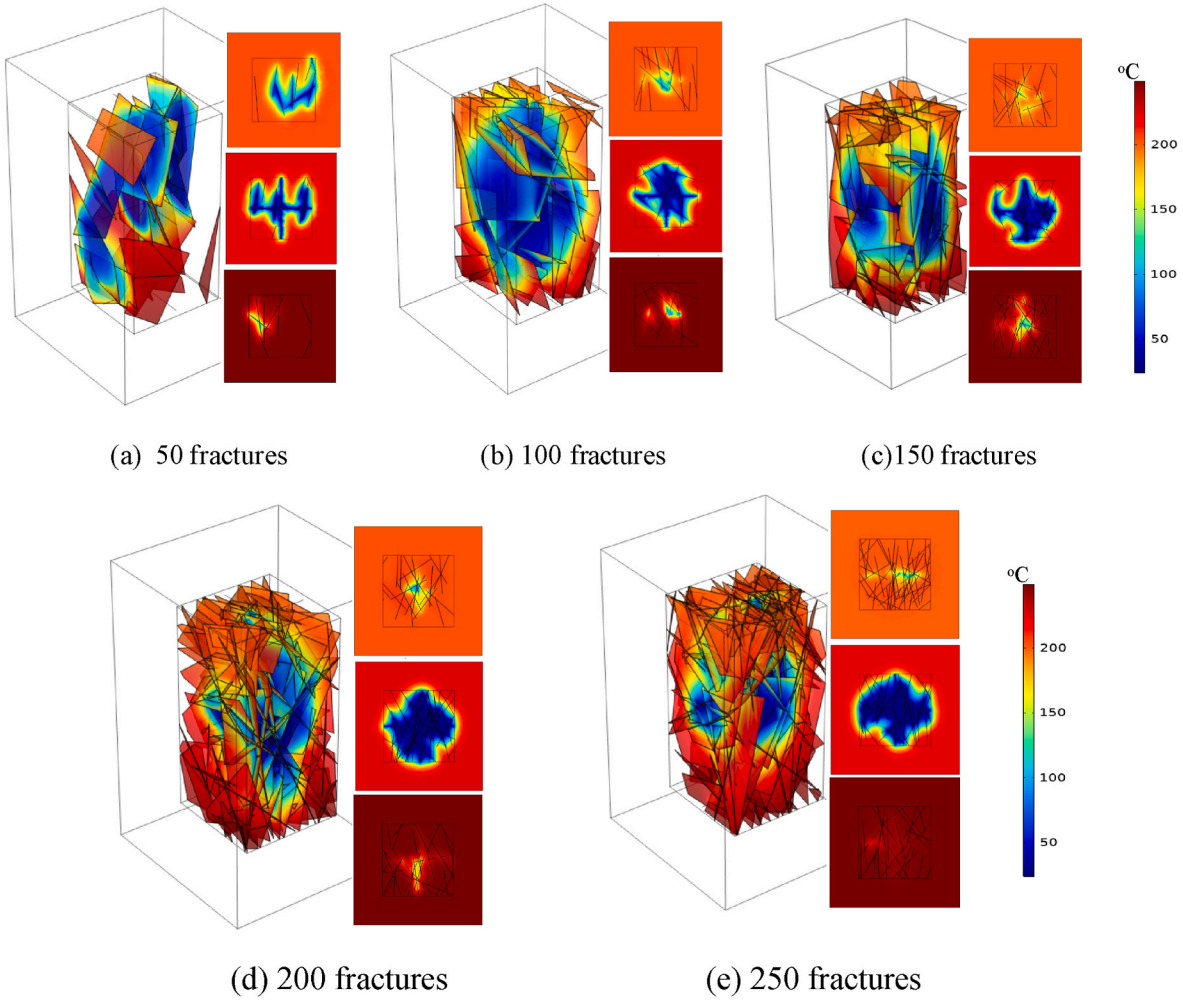


Fig. 10. Reservoir temperature variation with fracture number at different production times ($q = 60$ kg/s, 4 branches).

different fracture numbers and the corresponding values at different times, respectively. Fig. 11(a) shows the variation of production temperature under different fracture numbers. When the number of fractures is 50, the production temperature is low due to the limited heat transfer area, and the value is 135 °C at 30 years. When the number of fractures is 100, the production temperature is 146 °C at 30 years. As the number of fractures continues to increase, the outlet temperature no longer increases significantly. Fig. 11(b) and (c) show the pressure difference and the pumping power, respectively. When the number of fractures is low, the pressure difference and pumping power are large. When the number of fractures is 50 and 100, the maximum pressure differences are 16.3 MPa and 11.5 MPa, respectively, and the maximum pumping powers are 1.39 MW and 0.99 MW, respectively. When the number of fractures is 150, the pumping power is reduced to 0.42 MW. As the number of fractures increases, the reduction in pumping power becomes less pronounced. Fig. 11(d) shows production power evolution for different fracture numbers. More fractures boost initial power, but with 50 fractures, power declines quickly. Power remains stable for 100-150 fractures, while 200-250 fractures show limited gains. Production power varies nonlinearly with the number of fractures, indicating that simply increasing fractures does not guarantee better performance. Optimizing fracture scales is key for efficient and sustainable EGS operation. The results are consistent with previous studies. Shi et al. [35] reported that excessive fractures may reduce production temperature by accelerating thermal breakthrough. Similarly, the randomly distributed fractures in this study can form interconnected high-permeability channels, shortening fluid residence time and promoting thermal short-circuiting. Once the fracture number exceeds a critical threshold, production temperature may therefore decline.

MCML-EGS power stops increasing beyond 200 fractures, so 50, 100, 150, and 200 fractures were chosen to compare heat extraction efficiency with ML-EGS. Fig. 12(a) compares the cumulative production of the MCML-EGS and ML-EGS under different numbers of fractures. MCML-EGS achieves higher cumulative production across all fracture numbers. With the increase in the number of fractures, the cumulative power of MCML-EGS increases by 21%52%, 36%, 21%, and 14% compared to ML-EGS. MCML-EGS connects more fractures and reduces the fluid resistance without adding another vertical main well. Consequently, the MCML-EGS achieves greater cumulative energy production. The maximum pressure differences during operation are compared in Fig. 12(b). Within the range of 50 to 200 fractures, the pressure difference of the MCML-EGS is consistently and significantly lower than that of the ML-EGS, with reductions ranging from 94.3% to 81.4%. This advantage is more pronounced when the fracture number is lower. This shows that the MCML-EGS effectively expands the seepage path and disperses the flow resistance through the synergistic effect of multi-layer injection-production and multi-branch wells, thereby greatly reducing the pumping power required for system operation. The MCML-EGS not only improves the heat extraction power but also reduces the required pumping power.

3.3.2. *Number of lateral branches*

Increasing the number of lateral branches enhances connectivity between the wellbore and fracture network, thereby improving heat

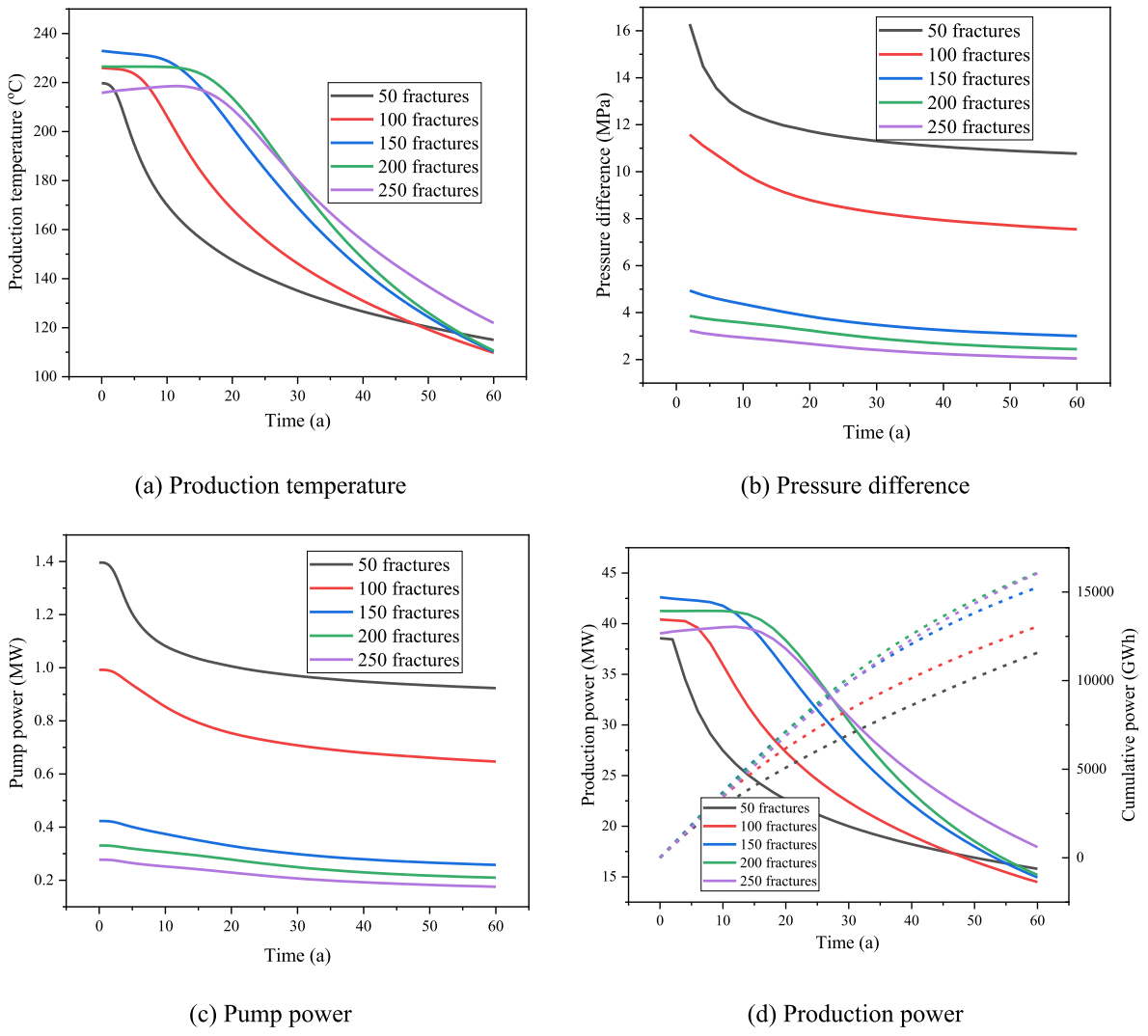


Fig. 11. Reservoir production power under different numbers of fractures (q = 60 kg/s, 4 branches).

Table 3
Production performance of MCML-EGS system for different numbers of fractures after 60 years.

Fracture number	Production temperature at 60 yr (°C)	Pressure at 0 yr (MPa)	Pressure at 60 yr (MPa)	Pump power at 0 yr (MW)	Pump power at 60 yr (MW)	Production power at 60 yr (MW)	Cumulative thermal energy production at 60 yr (GWh)
50	115.44	16.31	10.69	1.39	0.92	15.79	11577.3
100	109.56	11.52	7.46	0.99	0.65	14.48	13051.8
150	110.29	5.35	3.05	0.42	0.25	14.93	15256.4
200	111.03	3.92	2.38	0.33	0.21	15.18	16086.3
250	122.06	3.23	2.01	0.28	0.18	17.93	16054.2

extraction efficiency in MCML-EGS. This section systematically evaluates its impact by considering two to six lateral wells.

Fig. 13 and Table 4 show the variation of system power generation with the number of lateral wells and the cumulative energy production under different fracture numbers. The results show that when the fracture number is low (50 fractures), the response of production power to the number of lateral wells is relatively uncertain. Increasing the number of lateral wells does not lead to a consistent trend of increasing power, indicating that system performance is strongly constrained by fracture connectivity. Under moderate fracture density conditions (100-150 fractures), appropriately increasing the number of lateral wells (e.g., 4-5 wells) can significantly enhance system production power. This demonstrates that lateral wells can effectively connect more fractures involved in heat exchange, thereby expanding the effective heat exchange volume. However, in highly developed fracture networks (200 fractures), the marginal benefit of further increasing the number of lateral wells on power improvement is notably reduced. It may even exacerbate thermal short-circuiting effects by connecting to high-conductivity pathways, which is unfavorable for long-term stable heat production. The results reported in Ref. [36] showed that increasing the number of lateral branches could effectively improve heat extraction performance by enlarging the contact area between the working fluid and the reservoir. However, the enhancement gradually diminished with further increases in the number of branches due to the limited heat transfer region and increased flow interference among branches. These findings are consistent with the results of this study, where additional

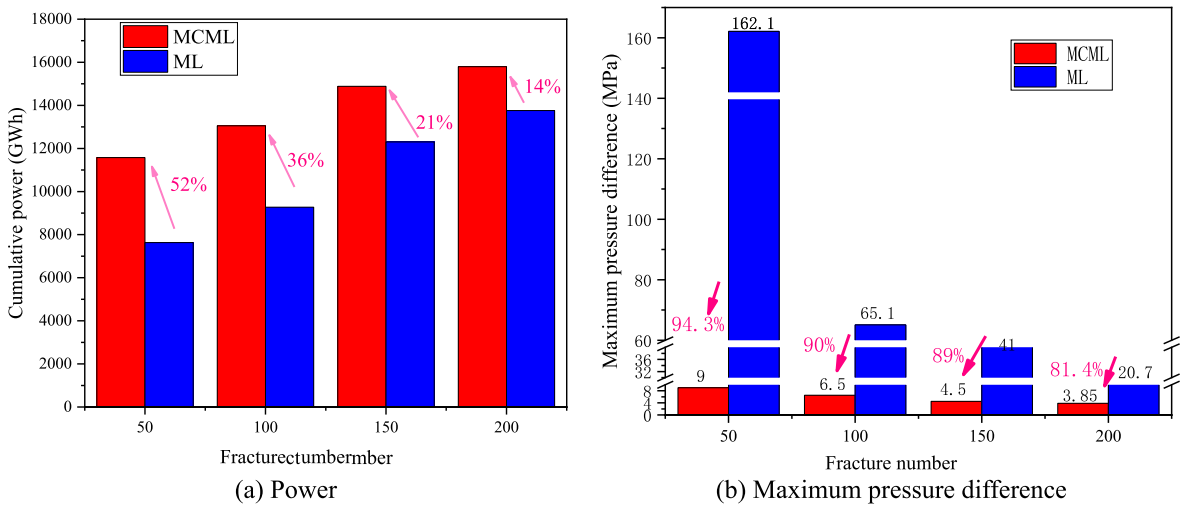


Fig. 12. Comparison of cumulative energy production and pressure difference between MCML-EGS and ML-EGS under different numbers of fractures.

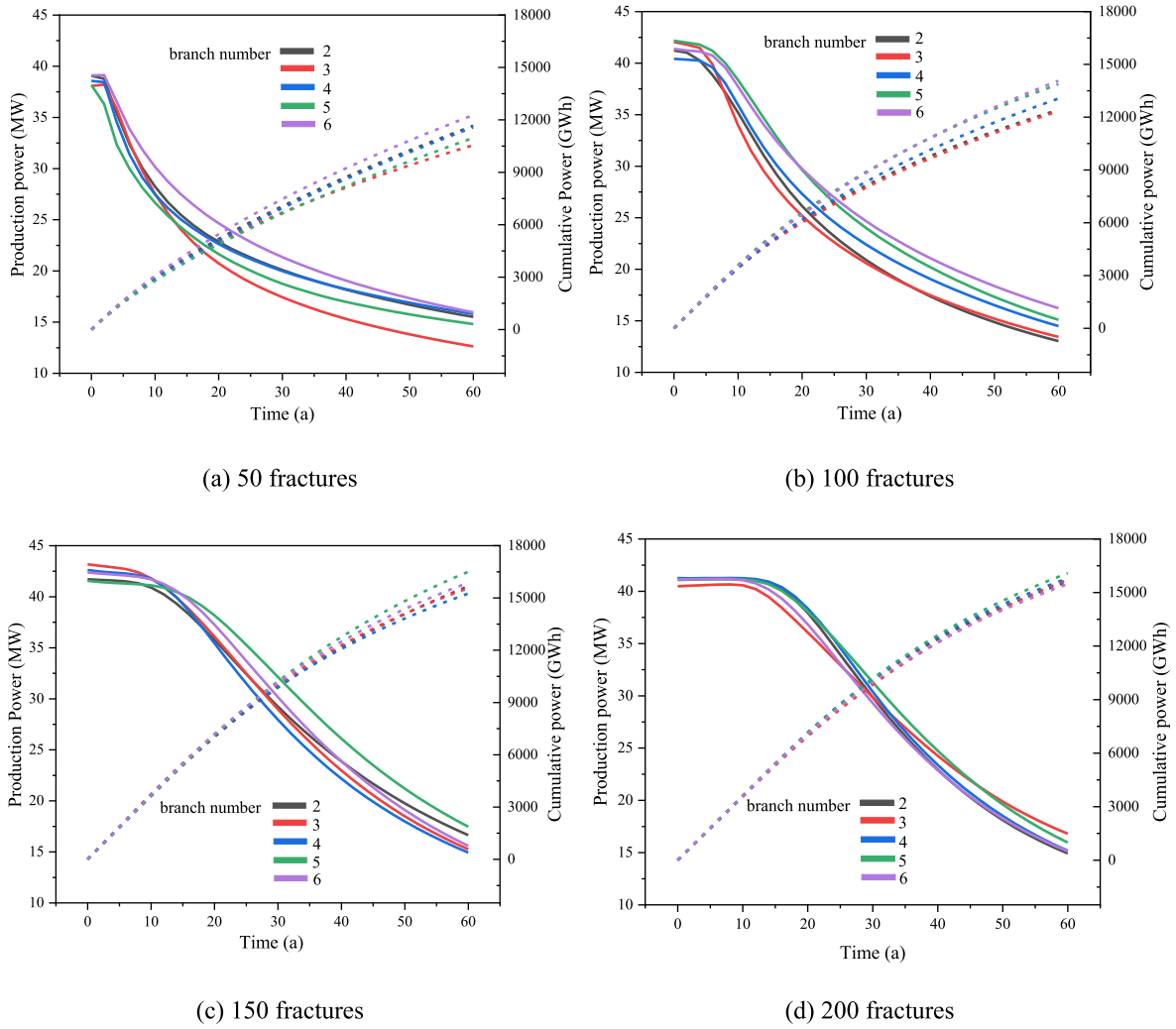


Fig. 13. Variation of production power over time under different fracture numbers and different numbers of lateral wells ($q = 60$ kg/s).

branches improve cumulative energy production, but the improvement becomes less significant when the branch number exceeds a certain range.

3.3.3. *Length of lateral wells*

Fig. 14 shows the relationship between production power and different lateral well lengths under different fracture numbers, and the cumulative energy production of the MCML-EGS for different lateral-

Table 4
Cumulative thermal energy production of the MCML-EGS for different numbers of lateral wells and fractures.

Branch number	Cumulative thermal energy production (GWh)			
	50 fractures	100 fractures	150 fractures	200 fractures
2	12211.6	12273.3	15888.5	15769.4
3	11055.7	12713.1	15776.7	15861.7
4	11577.3	13051.8	15256.4	16086.3
5	11476.4	14374.8	16670.5	16178.6
6	12733.6	12942.4	16026.3	15567.2

well lengths and fracture numbers. For 50 fractures, the cumulative energy production increases only from 980 GWh to 1696 GWh when the lateral well length increases from 100 to 150 m. This is an increase of approximately 42%. When the lateral well length is further increased to 200 m, the power suddenly increases to 10,917 GWh, an increase of more than 585%, indicating that there is a critical branch length in a sparsely fractured reservoir. Gao et al. [34] also pointed out that increasing the number of branch wells provides only limited improvement in production temperature in multilateral-well geothermal systems within complex fractured reservoirs. An excessive number of lateral wells may not further enhance heat extraction and can even adversely affect the production temperature. The system's heat-transfer capacity is fully utilized only when the lateral branch effectively connects the principal flow-conducting fractures. In the case of 100 fractures, the power increases steadily from 9508 GWh to 14,734 GWh when the length of the lateral well increases from 50 m to 250 m in MCML-EGS, with an overall increase of about 54%. This increase indicates that the heat transfer volume of the extended branch can be continuously expanded when the fracture network is relatively developed. For 150-200 fractures, the power increases by about 34% and 24%, respectively, and the marginal benefit is significantly reduced. The underlying mechanism is that as flow becomes increasingly dominated by fractures, extending the lateral wells primarily connects to high-conductivity channels, leading to limited growth or even saturation of the heat exchange volume.

3.3.4. *Injection rate*

Fig. 15 shows the variation of MCML-EGS production power at different injection rates and fracture numbers, and the cumulative energy production of the MCML-EGS under different water injection rates and fracture numbers. The results show that when the fracture number remains unchanged, the production power increases with the injection rate. At low injection rates, the production power is more sensitive to changes in the injection rate. As the injection rate increases, production power increases substantially. When the injection rate exceeds about 100 kg/s, the growth rate of production power slows significantly. Zhang et al. [37] pointed out that among the controllable parameters, injection mass flow rate has the greatest influence on power generation. Increasing the injection flow rate can significantly increase power generation, but a reasonable combination of parameters is needed, rather than simply increasing the flow rate indefinitely. Furthermore, increasing the injection rate leads to a significant rise in the

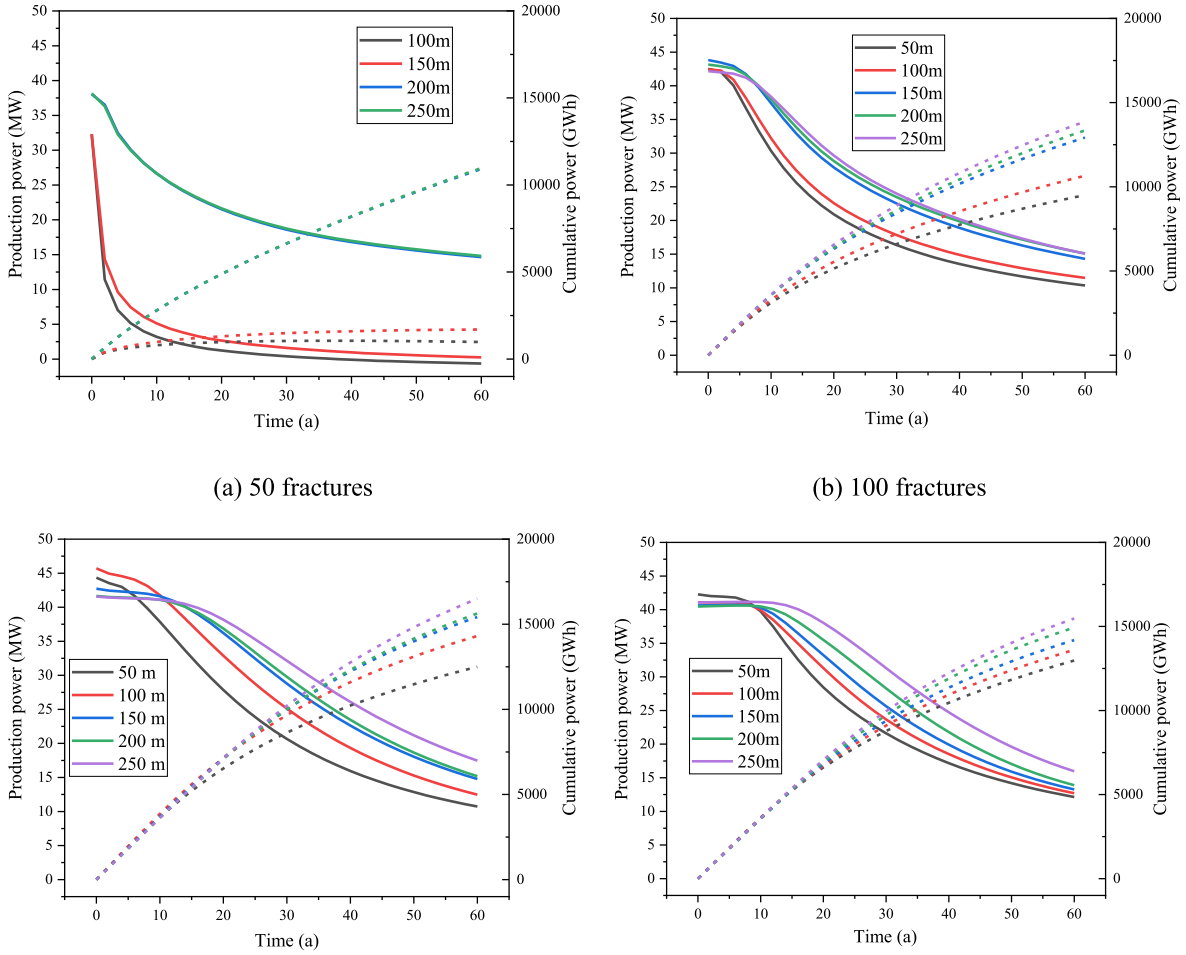


Fig. 14. Variation of production power with lateral well length under different fracture numbers.

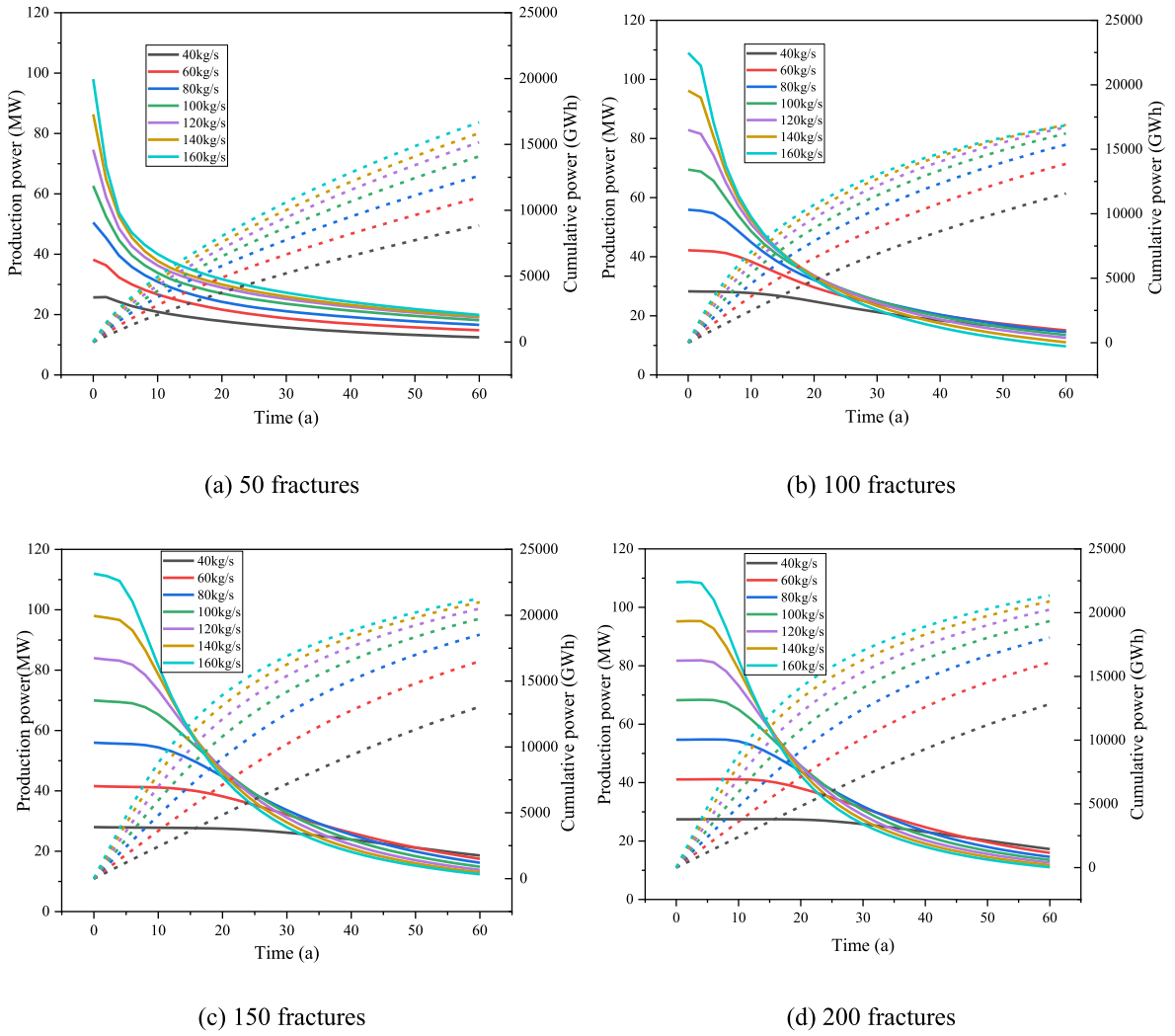


Fig. 15. Variation of production power over time under different injection rates (N = 5 lateral wells, L = 250 m).

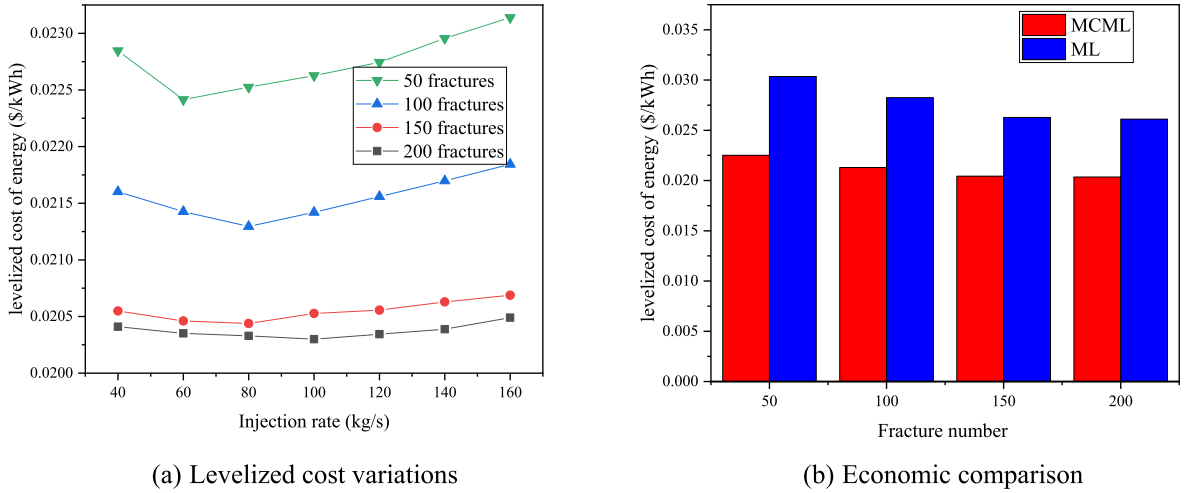


Fig. 16. (a) Levelized cost variations with injection rate for different total numbers of fractures; (b) Economic comparison of MCML-EGS and ML-EGS.

injection-production pressure difference and circulating pump energy consumption, while the marginal gain in production power diminishes. This indicates that continuously improving the system economy through injection rate alone is not feasible.

4. Economic analysis

Section 4 demonstrates that the MCML-EGS achieves maximum production power with five branch wells, each 250 m in length.

Table 5
Economic analysis of different geothermal development methods.

Geothermal system	Well layout	fracture	LCOE	Sources
Multi-well EGS	Pinnate well	Parallel fracture	0.035 $/kWh	Xie and Wang [38]
	Multiple vertical wells	DFN fracture	0.0341 $/kWh	Li et al. [39]
	Doublet wells	DFN fracture	0.035 $/kWh	Zhong et al. [40]
	Three horizontal wells	Parallel fracture	0.047 $/kWh	Lei et al. [40]
	Three vertical wells	Dual porosity method	0.037 $/kWh	Li et al. [41]
	Two horizontal wells	Dual porosity method	0.0413 $/kWh	Zhang et al. [20]
SCGS	Single U-shape well	No fracture	0.335 $/kWh	Sun et al. [42]
	Single horizontal well	No fracture	0.265 $/kWh	Wang et al. [43]
ML-EGS	Single main well	DFN fracture	0.0213 $/kWh	This study
MCML-EGS	Single main well	DFN fracture	0.0204 $/kWh	This study

Although production power increases with injection rate, so does the injection pumping-power consumption. Based on Eqs. (21)–(28), the total cost of the MCML-EGS system under various operating conditions was calculated, and its economic performance was evaluated for different fracture numbers and injection rates. Economic analysis (Fig. 16(a)) reveals that the overall economics of the MCML-EGS are jointly governed by fracture scale and operating parameters. At a fixed injection rate, the unit electricity cost decreases significantly with increasing fracture number. As the fracture number increases from 50 to 200, the unit cost drops from approximately 0.0224-0.0231 to 0.0203-0.0205 $/kWh, a reduction of roughly 10-12%, indicating that greater fracture development substantially improves energy recovery efficiency. For a given fracture number, the unit electricity cost first decreases and then gradually increases with injection rate, reaching its minimum at 60-80 kg/s. With 200 fractures, the unit cost can be as low as approximately 0.0203 $/kWh, reflecting an optimal balance between power generation gains and pump energy consumption at moderate injection rates. In summary, enhancing fracture development and optimizing the injection rate are the two key strategies for reducing the levelized cost of electricity and improving the economic feasibility of the MCML-EGS.

The MCML-EGS is more economical than ML-EGS (Fig. 16(b)). Its levelized cost of energy (LCOE) is reduced by approximately 25.7%, primarily due to the substantial savings in drilling investment resulting from the single-well structure and the reduced pump operating costs caused by an 81%-94% reduction in injection-production pressure difference.

Table 5 compares the levelized cost of energy (LCOE) of different geothermal systems. Conventional multi-well EGS exhibits an LCOE of 0.034–0.047 $/kWh, while single-well closed-loop geothermal systems (SCGS) without fractures reach 0.265–0.335 $/kWh due to low heat exchange efficiency. The proposed MCML-EGS achieves the lowest LCOE of 0.0204 $/kWh, outperforming ML-EGS (0.0213 $/kWh). MCML-EGS significantly improves economic viability compared to the previously proposed system.

5. Discussions

The model provides useful insights into the thermal performance of the proposed coaxial well system. The novel system is also promising in scenarios such as energy storage and CO2 geological sequestration [44,45]. Several limitations remain. Wellbore heat transfer, including conduction through the tubing and casing and convective heat exchange between the inner pipe and annulus, was neglected. In addition, reservoir heterogeneity, anisotropy, and fracture connectivity may cause substantial uncertainty in production [46], none of which were explicitly considered here. These assumptions may lead to deviations between the predicted and actual outlet temperature and heat extraction performance. Future work will develop a coupled wellbore-reservoir model incorporating wellbore heat loss, reservoir heterogeneity, and transient operating conditions. The thermal production uncertainty will be quantified to support reliable prediction and evaluation of long-term geothermal production.

6. Conclusions

A novel MCML-EGS based on a single multi-casing coaxial well with multilateral branches was proposed and evaluated. It enlarged the effective heat-exchange volume, improved long-term output stability, and reduced the risk of premature thermal breakthrough. Over a 60-year operation period, the cumulative energy production of the MCML-EGS increased by approximately 14%-52% compared with that of the ML-EGS under different fracture-number conditions. At the same injection rate, the injection-production pressure difference was reduced by 81%-94%, which lowered the circulating-pump demand and improved the overall energy efficiency.

Increasing the fracture number enlarged the heat-exchange area and enhanced the initial thermal output, with an approximate optimal range of 150-200 fractures under the investigated conditions. Beyond this range, the marginal power gain decreased, and uneven fluid distribution increased the possibility of thermal short-circuiting. The highest production power was obtained when five branch wells with a length of 250 m were employed, while an appropriate injection rate provided a better balance between heat extraction and pumping consumption. By increasing cumulative energy production and reducing pumping-power consumption, the MCML-EGS achieved a lower levelized cost of energy and demonstrated favorable economic potential for geothermal development.

CRediT authorship contribution statement

Guoying Wang: Writing – original draft, Methodology, Funding acquisition, Formal analysis, Conceptualization. **Xingyu Liu:** Writing – original draft, Investigation, Formal analysis. **Guofeng Song:** Writing – review & editing, Methodology, Investigation. **Wenyuan Jiang:** Writing – review & editing, Validation. **Housheng Jia:** Supervision, Project administration, Funding acquisition. **Songlin Guo:** Investigation, Data curation. **Norbert Klitzsch:** Visualization. **Chuanliang Yan:** Resources. **Shaowei Liu:** Resources, Funding acquisition.

Declaration of competing interest

The authors declare that they have no known competing financial interests or personal relationships that could have appeared to influence the work reported in this paper.

Acknowledgments

This study was funded by the National Natural Science Foundation of China (52104128, 52274078, 52104143, 52374099), the National Key Research and Development Program of China (2019YFA0705501), Key R&D and Promotion Projects in Henan Province (252300420035), Henan Provincial Science and Technology Research Project (252102320320, 252102320330), and Research Project on Experimental Teaching and Teaching Laboratory Construction of the Ministry of Education (SYJX2024-131).

Appendix A. Supplementary data

Supplementary data to this article can be found online at https://doi.org/10.1016/j.renene.2026.126549.

References

[1] P. Asai, P. Panja, J. McLennan, J. Moore, Performance evaluation of enhanced geothermal system (EGS): surrogate models, sensitivity study and ranking key parameters, Renew. Energy 122 (2018) 184–195.
[2] X. Song, G. Wang, Y. Shi, R. Li, Z. Xu, R. Zheng, Y. Wang, J. Li, Numerical analysis of heat extraction performance of a deep coaxial borehole heat exchanger geothermal system, Energy 164 (2018) 1298–1310.
[3] P.J. Roache, Perspective: a Method for Uniform Reporting of Grid Refinement Studies, 1994.
[4] Y. Zhang, C. Yu, G. Li, X. Guo, G. Wang, Y. Shi, C. Peng, Y. Tan, Performance analysis of a downhole coaxial heat exchanger geothermal system with various working fluids, Appl. Therm. Eng. 163 (2019).
[5] J. Liu, P. Zhao, J. Peng, H. Xian, Insight into the investigation of heat extraction performance affected by natural fractures in enhanced geothermal system (EGS) with THM multiphysical field model, Renew. Energy 231 (2024).
[6] D. Xiao, C. Cai, H. Tang, L. Li, Y. Hu, J. Liu, R. Yang, Research on economic length of the horizontal section of downhole coaxial heat exchanger geothermal system based on net present value, Int. J. Energy Res. 46 (5) (2021) 6351–6369.
[7] Y. Shi, X. Song, G. Li, R. Li, Y. Zhang, G. Wang, R. Zheng, Z. Lyu, Numerical investigation on heat extraction performance of a downhole heat exchanger geothermal system, Appl. Therm. Eng. 134 (2018) 513–526.
[8] G. Song, X. Song, G. Li, Y. Shi, G. Wang, J. Ji, F. Xu, Z. Song, An integrated multi-objective optimization method to improve the performance of multilateral-well geothermal system, Renew. Energy 172 (2021) 1233–1249.
[9] G. Wang, X. Song, Y. Shi, B. Sun, R. Zheng, J. Li, Z. Pei, H. Song, Numerical investigation on heat extraction performance of an open loop geothermal system in a single well, Geothermics 80 (2019) 170–184.
[10] X. Song, Y. Shi, G. Li, R. Yang, G. Wang, R. Zheng, J. Li, Z. Lyu, Numerical simulation of heat extraction performance in enhanced geothermal system with multilateral wells, Appl. Energy 218 (2018) 325–337.
[11] L. Tian, Y. Su, H. Huang, Numerical evaluation of the heat extraction performance of single-well enhanced geothermal system with rough fractures, Int. J. Heat Mass Tran. 256 (2026) 127980.
[12] M. Qiao, Y. Zhou, Z. Jing, C. Feng, L. Zheng, L. Wang, R. Xue, Heat extraction analysis of an innovative single-well open-loop geothermal system using scCO2, Energy 328 (2025) 136502.
[13] Y. Shi, X. Song, G. Wang, J. McLennan, B. Forbes, X. Li, J. Li, Study on wellbore fluid flow and heat transfer of a multilateral-well CO2 enhanced geothermal system, Appl. Energy 249 (2019) 14–27.
[14] M. Qiao, Z. Jing, C. Feng, M. Li, C. Chen, X. Zou, Y. Zhou, Review on heat extraction systems of hot dry rock: classifications, benefits, limitations, research status and future prospects, Renew. Sustain. Energy Rev. 196 (2024) 114364.
[15] J. Liao, K. Hu, F. Mehmood, B. Xu, Y. Teng, H. Wang, Z. Hou, Y. Xie, Embedded discrete fracture network method for numerical estimation of long-term performance of CO2-EGS under THM coupled framework, Energy 285 (2023) 128734.
[16] G. Song, Y. Shi, F. Xu, X. Song, G. Li, G. Wang, Z. Lv, The magnitudes of multi-physics effects on geothermal reservoir characteristics during the production of enhanced geothermal system, J. Clean. Prod. 434 (2024) 140070.
[17] X. Zhang, Z. Huang, G. Li, X. Wu, T. Wang, X. Zhou, Enhancing reservoir stimulation and heat extraction performance for fractured geothermal reservoirs: utilization of novel multilateral wells, Energy 291 (2024) 130410.
[18] X. Hou, X. Zhong, S. Nie, Study on the heat recovery behavior of horizontal well systems in the Qiabuqia geothermal area, Energy 286 (2024) 129424.
[19] L. Wang, H. Li, Y. Gong, X. Bu, Numerical simulation of single-well enhanced geothermal power generation system based on discrete fracture model, Geothermics 120 (2024) 103001.
[20] Y. Zhang, Y. Zhang, L. Zhou, Z. Lei, L. Guo, J. Zhou, Reservoir stimulation design and evaluation of heat exploitation of a two-horizontal-well enhanced geothermal system (EGS) in the Zhacang geothermal field, Northwest China, Renew. Energy 183 (2022) 330–350.
[21] M.L. McLean, D.N. Espinoza, B. Ahmmed, The impact of effective fractured rock mass properties on development of flow channeling in enhanced geothermal systems, Renew. Energy 237 (2024).
[22] X. Liang, T. Xu, J. Chen, Z. Jiang, A deep-learning based model for fracture network characterization constrained by induced micro-seismicity and tracer test data in enhanced geothermal system, Renew. Energy 216 (2023).
[23] X. Gao, Y. Zhang, Y. Cheng, Z. Yu, Z. Hu, Y. Huang, Heat extraction performance of fractured geothermal reservoirs considering aperture variability, Energy 269 (2023) 126806.
[24] B. Jia, Q. Wang, Z. Huang, Thermal depletion patterns of CO2 and water in closed-loop coaxial geothermal systems with vertical and L-shaped wells, Renew. Energy 274 (2026).
[25] X. Hu, J. Banks, Y. Guo, W.V. Liu, Retrofitting abandoned petroleum wells as doublet deep borehole heat exchangers for geothermal energy production—a numerical investigation, Renew. Energy 176 (2021) 115–134.
[26] S. Erol, V. Harcouët-Menou, B. Laenen, P. Bayer, Efficiency of single-well geothermal systems with multi-lateral drills, Geothermics 89 (2021) 101928.
[27] S. Mu, A. Zhang, L. Zhao, Investigation on the heat extraction performance considering a rough fracture network in heterogeneous reservoirs, Renew. Energy 233 (2024) 121160.
[28] P. Yu, D. Dempsey, R. Archer, A three-dimensional coupled thermo-hydro-mechanical numerical model with partially bridging multi-stage contact fractures in horizontal-well enhanced geothermal system, Int. J. Rock Mech. Min. Sci. 143 (2021) 104787.
[29] S.K. Sanyal, Cost of geothermal power and factors that affect it. Proceedings of World Geothermal Congress, 2005, pp. 24–29.
[30] J. Chen, F. Jiang, Designing multi-well layout for enhanced geothermal system to better exploit hot dry rock geothermal energy, Renew. Energy 74 (2015) 37–48.
[31] Z. Ye, J.G. Wang, B. Hu, Comparative study on heat extraction performance of geothermal reservoirs with presupposed shapes and permeability heterogeneity in the stimulated reservoir volume, J. Petrol. Sci. Eng. 206 (2021) 109023.
[32] Z. Lei, Y. Zhang, S. Zhang, L. Fu, Z. Hu, Z. Yu, L. Li, J. Zhou, Electricity generation from a three-horizontal-well enhanced geothermal system in the Qiabuqia geothermal field, China: slickwater fracturing treatments for different reservoir scenarios, Renew. Energy 145 (2020) 65–83.
[33] Z. Xie, D. Han, J. Li, K. Li, A state-of-the-art review of hydraulic fracturing in geothermal systems, Sustainability 16 (24) (2024) 11087.
[34] X. Gao, Y. Zhang, Y. Huang, Y. Ma, Y. Zhao, Q. Liu, Study on heat extraction considering the number and orientation of multilateral wells in a complex fractured geothermal reservoir, Renew. Energy 177 (2021) 833–852.
[35] Y. Shi, X. Song, J. Li, G. Wang, R. Zheng, F. YuLong, Numerical investigation on heat extraction performance of a multilateral-well enhanced geothermal system with a discrete fracture network, Fuel 244 (2019) 207–226.
[36] Y. Shi, X. Song, G. Wang, J. Li, L. Geng, X. Li, Numerical study on heat extraction performance of a multilateral-well enhanced geothermal system considering complex hydraulic and natural fractures, Renew. Energy 141 (2019) 950–963.
[37] C. Zhang, G. Jiang, X. Jia, S. Li, S. Zhang, D. Hu, S. Hu, Y. Wang, Parametric study of the production performance of an enhanced geothermal system: a case study at the Qiabuqia geothermal area, northeast Tibetan plateau, Renew. Energy 132 (2019) 959–978.
[38] J. Xie, J. Wang, Numerical analysis and economic evaluation of pinnate horizontal well for supercritical CO2-based enhanced geothermal system, Geothermics 116 (2024) 102850.
[39] X. Li, J. Wang, C. Du, J. Luo, W. Gong, Performance analysis of heat extraction in a multi-well EGS using a DFN-based modeling scheme, Appl. Therm. Eng. 269 (2025) 125988.
[40] C. Zhong, T. Xu, Y. Yuan, B. Feng, H. Yu, The feasibility of clean power generation from a novel dual-vertical-well enhanced geothermal system (EGS): a case study in the Gonghe Basin, China, J. Clean. Prod. 344 (2022) 131109.
[41] T. Li, Y. Qiao, K. Zhou, J. Li, X. Gao, Techno-economic and environmental performance of combined heat and power for hot dry rock based on life cycle assessment, Renew. Energy 242 (2025) 122399.
[42] F. Sun, Y. Yao, G. Li, X. Li, Geothermal energy development by circulating CO2 in a U-shaped closed loop geothermal system, Energy Convers. Manag. 174 (2018) 971–982.
[43] G. Wang, X. Song, Y. Shi, F. Yulong, R. Yang, J. Li, Comparison of production characteristics of various coaxial closed-loop geothermal systems, Energy Convers. Manag. 225 (2020) 113437.
[44] Y. Shi, Q. Cui, X. Song, G. Li, G. Wang, Performances of a novel compressed CO2 energy storage and heat storage integration system using multi-stage hydraulic fractures of horizontal well in subsurface reservoirs, Renew. Energy 251 (2025) 123396.
[45] Q. Cui, Y. Shi, S. Li, X. Song, B. Zhu, G. Wang, J. Peng, Study on impacts of seasonal heat storage on CO2 geological sequestration and parameter optimization, Energy (2025) 137698.
[46] G. Song, S. Geiger, D. Voskov, H.A. Abels, P.J. Vardon, Scenario-based data assimilation framework to improve production estimates for geologically complex geothermal reservoirs, Geoenergy Sci. Eng. 263 (2026) 214490.